Separation and Purification Technology 317 (2023) 123860

Contents lists available at ScienceDirect

Separation and Purification Technology

journal homepage: www.elsevier.com/locate/seppur

Insights into boron accelerated Fenton-like chemistry: Sustainable and fast Fe^{III}/Fe^{II} circulation

Peng Zhou [a,b,c], Shuang Meng [a,b], Minglu Sun [a,b], Kunsheng Hu [c], Yangyang Yang [c], Bo Lai [a,b,*], Shaobin Wang [c], Xiaoguang Duan [c,*]

[a] State Key Laboratory of Hydraulics and Mountain River Engineering, College of Architecture and Environment, Sichuan University, Chengdu 610065, China
[b] Sino-German Centre for Water and Health Research, Sichuan University, Chengdu 610065, China
[c] School of Chemical Engineering, The University of Adelaide, Adelaide, SA 5005, Australia

ARTICLE INFO

Keywords:
Fenton-like reaction
Boron
Oxidation
Radicals
Co-catalyst

ABSTRACT

In this work, amorphous boron (A-Boron) as a metal-free co-catalyst was applied to address the slow kinetics of Fe^{II} regeneration and inactive Fe^{III} accumulation in Fenton-like peroxydisulfate (PDS) activation. The A-Boron/Fe^{III}/PDS system can rapidly degrade bisphenol A (BPA) for ten cyclic runs without performance decline. Based on chemical probing, radical quenching and in situ capturing tests, Fe(IV) and radicals ($^{\cdot}OH$ and $SO_4^{\cdot-}$) are identified as the primary reactive species, and the combined ROS can achieve universal pollutants oxidation with high PDS utilization efficiency. QSAR study unveils that the k_{obs} values of pollutants linearly depend on their E_{HOMO}. A-Boron can bind with Fe^{III} species for catalytic reduction, and meanwhile, the semi-metallic surface experiences stepwise transformation. The fast dissolution of inactive surface boron oxide enabled a self-cleaned and reactive boron surface for long-lasting iron circulation. Also, BPA degradation pathways were proposed based on UHPLC-QTOF-MS tests and Fukui index calculation.

1. Introduction

Peroxydisulfate (PDS)-based advanced oxidation technologies (AOTs) can produce reactive oxygen species (ROS) to degrade a broad spectrum of microcontaminants, such as antibiotics, endocrine disrupting chemicals, and antibiotic resistance genes [1–3]. The activation and cleavage of peroxide bonds of PDS typically require high energy input (e.g., ultraviolet light and ultrasound) for homolysis or electron donor/sacrificer (e.g., cobalt, copper, and iron) for heterolysis [4–7]. Particularly, ferrous species (Fe^{II}) is not only a benchmark catalyst in Fenton oxidation (Fe^{II}/H_2O_2), but also an effective activator to rapidly decompose PDS to produce ROS (e.g., hydroxyl radical ($^{\cdot}OH$) and sulfate radical ($SO_4^{\cdot-}$)) via Eqs. (1)–(3) [8,9]. Fe^{II} has a high practical potential due to the low cost ($70 ~ 80 per ton) and environmental friendliness of the parent salt (ferrous sulfate), and the subsequent coagulation and precipitation processes to recycle Fe^{III} species can further remove microcontaminants and their derivatives [10]. Different from the Fenton-like reaction between PDS and Fe^{II} through single electron transfer to generate $SO_4^{\cdot-}$ (Eq. (1)), PDS can also induce two electrons oxidation of Fe^{II} to produce a reactive Fe^{IV}-oxo complex ($Fe^{IV}O^{2+}$, Fe(IV)) via Eq. (4) [11–13]. Although the Fe^{II}/PDS system can produce abundant ROS and promptly oxidize organic contaminants with sufficient Fe^{II} at the initial stage, the fast and stoichiometric accumulation of Fe^{III} and sluggish kinetics of Fe^{II} regeneration dramatically limit the sustainable generation of ROS during long-term operation [14,15].

$$Fe^{II} + S_2O_8^{2-} \rightarrow Fe^{III} + SO_4^{\cdot-} + SO_4^{2-} \quad k = 27\ M^{-1}\cdot s^{-1} \tag{1}$$

$$SO_4^{\cdot-} + H_2O \rightarrow SO_4^{2-} + {}^{\cdot}OH + H^+ \quad k = 2 \times 10^{-3}\ M^{-1}\cdot s^{-1} \tag{2}$$

$$SO_4^{\cdot-} + OH^- \rightarrow SO_4^{2-} + {}^{\cdot}OH \quad k = 6.5 \times 10^7\ M^{-1}\cdot s^{-1} \tag{3}$$

$$Fe^{II} + S_2O_8^{2-} + H_2O \rightarrow Fe^{IV}O^{2+} + 2SO_4^{2-} + 2H^+ \quad k = 20\ M^{-1}\cdot s^{-1} \tag{4}$$

$$Fe^{III} + S_2O_8^{2-} \rightarrow Fe^{II} + S_2O_8^{\cdot-} \tag{5}$$

To overcome this inherent bottleneck of Fenton/Fenton-like processes, Chen et al. firstly added hydroxylamine to accelerate Fe^{III} reduction, resulting in fast and sustainable oxidation of benzoic acid [16]. Since then, many attempts have been made by coupling various electron sacrificers and the iron/PDS system to facilitate the circulation

* Corresponding authors at: State Key Laboratory of Hydraulics and Mountain River Engineering, College of Architecture and Environment, Sichuan University, Chengdu 610065, China (B. Lai).
E-mail addresses: laibo@scu.edu.cn (B. Lai), xiaoguang.duan@adelaide.edu.au (X. Duan).

https://doi.org/10.1016/j.seppur.2023.123860
Received 15 February 2023; Received in revised form 3 April 2023; Accepted 12 April 2023
Available online 17 April 2023

of Fe^{III}/Fe^{II} redox couples and achieve fast contaminant oxidation, such as metal sulfides, *L*-cysteine, *L*-ascorbic acid, and sodium sulfite [14,15]. The strategy of using reducing agents remarkably expedite Fenton-like oxidation. However, there are two main limitations that significantly discourage the scientific progress of this strategy toward practical application: (1) secondary organic or metal pollution caused by the decomposition of electron sacrificers, such as metal leaching, nitrogen-contained intermediates and low-molecular-weight organic acids [17–19]; (2) ROS quenching by reducing agents and their derivatives (e.g., k(•OH, *L*-cysteine) = 1.9×10^{10} $M^{-1}{\cdot}s^{-1}$; k(•OH, hydroxylamine) = 9.5×10^{9} $M^{-1}{\cdot}s^{-1}$; $k(SO_4^{\bullet-}$, hydroxylamine) = 8.5×10^{8} $M^{-1}{\cdot}s^{-1}$) [20,21]. Therefore, in search for ideal electron sacrificers is an urgent task for developing sustainable Fenton-like systems.

Boron between carbon and beryllium in the periodic table is a metalloid and possesses five electrons with specific electronic configuration ($1s^2$ $2s^2$ $2p^1$) [22]. The radiuses of two electrons in the 2s orbital are similar to the single electron in p orbital. Thus, the excitation of one 2s electron can easily occur to generate multiple-centered and electron-sharing bonds. This characteristic endows the high reactivity of boron atoms to combine with other nonmetal and metal elements [23–26]. Low valent boron atoms (B^0, B^I, and B^{II}) on the surface of boron powder thus can combine with Fe^{III} species (e.g., Fe^{3+}, $FeOH^{2+}$, and $Fe(OH)_2^+$) to rapidly produce Fe^{II} via electron migration [27]. Therefore, boron is a promising co-catalyst for promoting iron-catalyzed Fenton-like activation of PDS without concerns of leaching of organic and metal intermediates. Meanwhile, as a heterogeneous co-catalyst, the mass transfer limitation of nonporous boron may alleviate the co-catalyst-induced ROS quenching and avoid ineffective PDS consumption and improve chemical utilization efficiency.

Here, amorphous boron (A-Boron) was employed to boost the iron-mediated PDS activation for degrading organic pollutants, while bisphenol A (BPA) was selected as the primary target compound. A-Boron can strongly boost the oxidation kinetics of the iron/PDS systems (Fe^{II}/PDS and Fe^{III}/PDS) and maintain high degradation performance for ten cyclic tests. The generation and contribution of ROS were analyzed by combined radical quenching, probing and capturing analysis. The quantitative structure–activity relationship (QSAR) between E_{HOMO} and the apparent rate constant (k_{obs}) of the oxidation of various organic compounds were further analyzed. Moreover, the mechanism of A-Boron boosted Fenton catalysis were investigated via analyzing the transformation of iron species and stepwise oxidation of boron. Also, degradation pathways of BPA were analyzed based on analysis of Fukui index (DFT calculation) and UHPLC-QTOF-MS.

2. Materials and methods

2.1. Materials and reagents

The analytical grade reagents, including peroxydisulfate (PDS), amorphous boron (A-Boron), ferrous sulfate (Fe^{II}), ferric sulfate (Fe^{III}), OXONE (PMS, $KHSO_5{\cdot}0.5KHSO_4{\cdot}0.5K_2SO_4$), tetrahydroxydiboron (THDB), boron trioxide (B_2O_3), boric acid, methyl phenyl sulfoxide (PMSO), terephthalic acid (TPA), 5,5-dimethyl-1-pyrolin-N-oxide (DMPO), tertiary butanol (TBA), ethanol (EtOH), methyl alcohol (MeOH), methyl phenyl sulfone ($PMSO_2$), 2-hydroxyterephthalic acid (HTPA), bisphenol A (BPA), nitrobenzene (NB), phenol (PE), sulfamethoxazole (SMX), ibuprofen (IBP), tetracycline (TC), rhodamine B (RB), diethyl phthalate (DEP), dimethyl phthalate (DMP), benzoic acid (BA), methylene blue (MB), hydrogen peroxide (H_2O_2, 30 wt%) hydroxylamine hydrochloride, sodium nitrate, sodium chloride, sodium hydroxide, sulfuric acid, and 1,10-phenanthroline, are purchased from Sigma-Aldrich (Australia).

2.2. Performance evaluation for degrading organic contaminants

Batch experiments for evaluating the reactivity of A-Boron to boost the iron/PDS system were performed in ultrapure water (100 mL) temperature-controlled by a water bath (25 ± 1 °C) with constant mechanical agitation (300 rpm). After adding 20 μM organic contaminant and desired dosage of PDS, solution pH was adjusted using sodium hydroxide and sulfuric acid before the reaction. All experiments were started by simultaneously adding A-Boron and iron salts (Fe^{II} or Fe^{III}) with desired dosages. Samples were withdrawn and filtered by microfiltration membranes (0.22 μm) to monitor organic pollutants, PDS as well as iron species. The ultra-high performance liquid chromatography (UHPLC, UltiMate 3000) was applied to detect the concentrations of organic contaminants (mixed with excess sodium thiosulfate and MeOH) (Text S1 and Table S1). The spectrophotometric methods were used to monitor the concentrations of PDS (mixed with potassium iodide) and iron species (chelated with 1,10-phenanthroline) (Text S2 and Text S3).

2.3. Qualitative and semi-quantitative analysis of reactive oxygen species

The qualitative identification of radicals was performed by electron paramagnetic resonance (EPR, Bruker EMX plus) (Text S4). Quenching tests using TBA and EtOH were carried out for analyzing the contributions of reactive radicals, because of the discrepant rate constants between different radicals and the alcohols. The semi-quantitative detection of hydroxyl radical with TPA as a chemical probe was also conducted by detecting the featured hydroxylated product of TPA (HTPA) using UHPLC methods [28]. Moreover, Fe(IV) species can oxidize PMSO to form $PMSO_2$ through a specific oxygen transfer route, which is intrinsically different from reactive radicals dominated oxidation of PMSO [11,13]. PMSO was employed as the chemical probe for qualitatively identifying Fe(IV) species and semi-quantitatively distinguishing the proportions of radical and nonradical pathways for contaminant oxidation in the A-Boron/Fe^{III}/PDS system by detecting PMSO depletion and $PMSO_2$ formation (Text S1 and Table S1).

2.4. Characterizations

The analysis of crystal structure and surface elements of original and residual A-Boron was carried out by X-ray diffraction (XRD, Bruker AXS D8 Advance), X-ray photoelectron spectroscopy (XPS, AXIS Ultra DLD), and near-edge X-ray absorption fine structure (NEXAFS) at the wiggler X-ray absorption structure (XAS) beamline (Australian Synchrotron in Melbourne). The structures and morphologies of original and reacted A-Boron powders were high-resolution transmission electron microscopy (HRTEM, JEOL JEM-2100F).

2.5. Quantitative structure–activity relationship (QSAR)

The apparent rate constants (k_{obs}) for removing contaminants obtained from the pseudo-first order kinetic model was coupled with their frontier orbital energies to set up the QSAR model. Based on the density functional theory (DFT), the chemical parameters (energy of the highest occupied molecular orbital (E_{HOMO}), lowest unoccupied molecular orbital (E_{LUMO}), and gap energy ($\Delta E = E_{LUMO}$-E_{HOMO})) of organic molecules were calculated using Gaussian 16 with calculation method of B3LYP and basis set of 6-311G (d, p).

2.6. Analysis of the oxidation pathway of BPA

The qualitative analysis of intermediates during BPA oxidation were performed by a UHPLC triple quadrupole time-of-flight mass spectrometry (UHPLC-QTOF-MS, Agilent G6545). The organic compounds derived from BPA were separated using a thermostatic autosampler consisting of a UHPLC system, a column chamber and a binary pump (Agilent 1290 series) equipped with a reverse-stage C_{18} analytical column. Fukui index (f_A^0, f_A^-, f_A^+) of BPA was calculated by Gaussian 16 based on DFT to further analyze the degradation pathway of BPA (Text S5).

3. Results and discussion

3.1. Efficacy of boron to boost Fenton-like PDS activation

The reactivity of A-Boron was evaluated in (Fe^{II}/PDS and Fe^{III}/PDS) systems for BPA oxidation. Fig. 1a depicts that Fe^{II} can effectively activate PDS to degrade BPA, and 30.3% of BPA was rapidly degraded in the Fe^{II}/PDS system at the first stage (within 2 min). But the low reactivity of PDS for Fe^{III} reduction limits the degradation of BPA at the second stage due to the exhaust of Fe^{II} [8]. To our delight, A-Boron significantly boosts the kinetics in Fe^{II}/PDS and Fe^{III}/PDS, and BPA was completely degraded within 20 min (Fig. 1a and 1b). A-boron can also strongly boost iron mediated Fenton-like systems for activating H_2O_2 and PMS, both systems of A-Boron/Fe^{III}/H_2O_2 and A-Boron/Fe^{III}/PMS can completely degrade BPA (Fig. S1). Therefore, A-Boron can boost the oxidation capability of Fenton-like activation of peroxides (H_2O_2, PDS, and PMS). Moreover, Fe^{III} was selected as a Fenton-like catalyst in subsequent experiments due to its high stability for storage and transport. The stability tests showed that A-Boron/Fe^{III}/PDS can maintain complete BPA removal within 20 min for 10 cycling tests (Fig. 1c), indicating a great potential for long-lasting operations.

3.2. Analysis of reactive oxygen species

3.2.1. Identification of reactive oxygen species

Multiple ROS can be produced via iron-catalyzed PDS decomposition, such as radicals ($SO_4^{\bullet-}$ and $^{\bullet}OH$) and Fe(IV) [11–13]. Fig. 2a depicts that 0.47 mM PDS was decomposed in the A-Boron/Fe^{III}/PDS system compared to less than 0.01 mM depletion of PDS in the Fe^{III}/PDS system, which implies the high activity of A-Boron to promote PDS decomposition. The evolved ROS were qualitatively identified by EPR tests (DMPO) and semi-quantitatively detected by radical quenching (TBA and EtOH) and chemical probe (TPA and PMSO) tests. The EPR spectrum in Fig. 2b demonstrates no characteristic signal appeared in the A-Boron/PDS system because A-Boron cannot directly activate PDS [29,30]. The EPR spectrum obtained from the Fe^{III}/PDS system without specific peaks of DMPO-radical adducts also reveals that the Fe^{III}/PDS system cannot directly produce reactive radicals. However, the distinct signals of DMPO-OH and DMPO-SO_4 adducts were detected in the spectrum obtained from the A-Boron/Fe^{III}/PDS system, implying that A-Boron enables the Fe^{III}/PDS system to produce $SO_4^{\bullet-}$ and $^{\bullet}OH$ [31–33]. In addition, the generation of 4.1 μM HTPA ($^{\bullet}OH$-induced hydroxylation product of TPA) further indicates the generation of $^{\bullet}OH$ by coupling A-Boron and the Fe^{III}/PDS system (Fig. 2c) [34].

Moreover, quenching tests with TBA and EtOH as radical quenchers were performed to analyze the contributions of reactive radicals ($SO_4^{\bullet-}$ and $^{\bullet}OH$) for the oxidation of BPA, resulting from the different rate constants of TBA and EtOH toward these radicals (Table 1). EtOH can effectively scavenge both radicals, whilst TBA only dominantly terminates $^{\bullet}OH$ oxidation [20,21]. Fig. 2d and Fig. S2 show that TBA can retard the BPA removal efficiency from 100% to 97.0% and k_{obs} decreases from 0.25 min^{-1} to 0.12 min^{-1}, implying the obvious contribution of $^{\bullet}OH$ for BPA oxidation. The addition of EtOH further inhibits BPA oxidation with 53.3% BPA removal in 30 min (k_{obs} of 0.02 min^{-1}), suggesting the critical role of $SO_4^{\bullet-}$ for BPA oxidation. Therefore, both $SO_4^{\bullet-}$ and $^{\bullet}OH$ can significantly degrade BPA in the A-Boron/Fe^{III}/PDS system.

3.2.2. Contributions of radical and nonradical pathways

Since EtOH did not completely terminate the oxidation, it is speculated that other reactive species may contribute to BPA removal. Despite lots of parallel efforts to analyze the ROS, the ongoing debate is the generation and contribution of high valent iron in Fe^{II}-catalyzed persulfate systems [11,13].

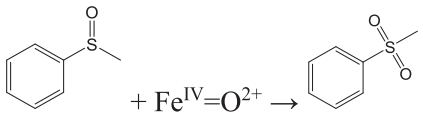

(6)

$$\Delta[PMSO] = \Delta[PMSO_2] + \Delta[PMSO\ (SO_4^{\bullet-})] + \Delta[PMSO\ (^{\bullet}OH)] \quad (7)$$

Recent literatures reported that Fe^{II}-mediated Fenton-like activation of PDS can produce reactive Fe(IV) (Eq. (4)) which possesses a high-spin state and can effectively oxidize some organic compounds [11–13]. Fe(IV) can oxidize sulfoxides (e.g., dimethyl sulfoxide and PMSO) to form corresponding sulfones via a featured oxygen transfer pathway, and the product is absent in radical oxidation [11,37]. Thus, the chemical probe tests using PMSO were carried out to qualitatively and semi-quantitatively identify the generation of Fe(IV) by monitoring the featured product of $PMSO_2$ (Eq. (6)). Meanwhile, this chemical probe can also distinguish the proportions of radical ($SO_4^{\bullet-}$ and $^{\bullet}OH$) and nonradical (Fe(IV)) pathways for PMSO oxidation [38].

Fig. 3a depicts that the Fe^{II}/PDS system can oxidize 30.1 μM PMSO and produce 13.9 μM $PMSO_2$ with a conversion efficiency of 46.4% ($\Delta[PMSO_2]/\Delta[PMSO]$). The addition of PDS apparently enhances PMSO oxidation (134.1 μM) and $PMSO_2$ generation (72.5 μM), and the A-Boron/Fe^{III}/PDS system attains a higher conversion efficiency from PMSO to $PMSO_2$ (54.1%). These results confirm that Fe(IV) is another vital reactive species accounting for pollutant degradation in the A-Boron/Fe^{III}/PDS system. Scheme 1 depicts the routes of the generation of these three types of ROS in the A-Boron/Fe^{III}/PDS system. Moreover, TBA was added to the A-Boron/Fe^{III}/PDS system to selectively terminate $^{\bullet}OH$-induced oxidation of PMSO, and thus the contributions of Fe(IV) and radicals for PMSO oxidation were assessed via Eq. (7). Hydroxyl radical, sulfate radical, and Fe(IV) contribute 12.7%, 33.2%, and 54.1% to PMSO oxidation at initial pH 3.1, respectively. Fig. 3b further reveals that a higher Fe^{III} concentration can accelerate ROS formation, and the percentage of Fe(IV)-mediated nonradical oxidation of PMSO increases from 53.2% to 63.1% with the augmented Fe^{III} dosage from 5 μM to 80 μM. Higher Fe^{III} dosage enables that the A-Boron/Fe^{III}/PDS system can

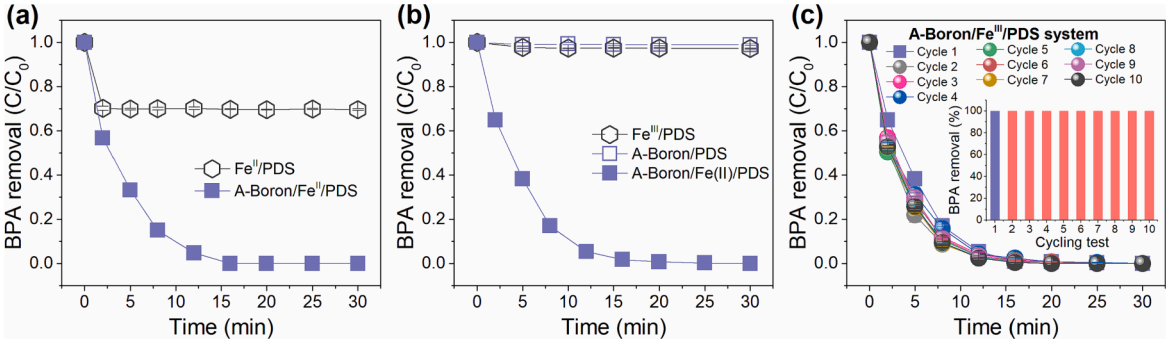

Fig. 1. Performance of A-Boron assisted (a) the Fe^{II}/PDS system and (b) the Fe^{III}/PDS system, (c) cycling tests in the A-Boron/Fe^{III}/PDS system. (A-Boron 100 mg/L, BPA 20 μM, initial pH 3.1, PDS 1.0 mM, Fe^{II} or Fe^{III} 20 μM).

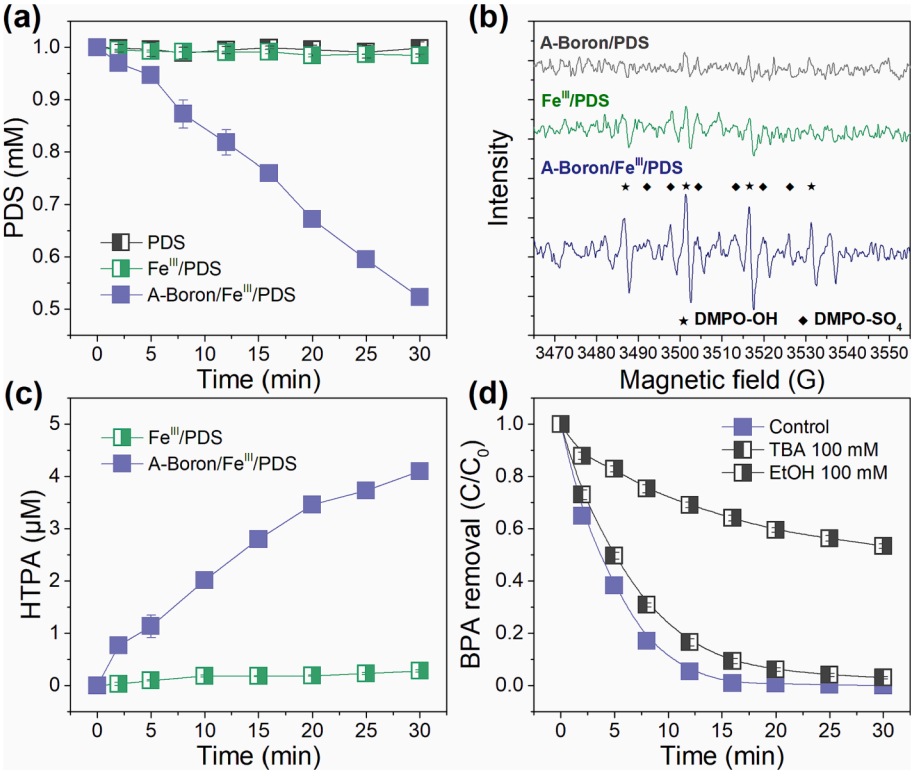

Fig. 2. (a) PDS decomposition, (b) EPR analysis, (c) generation of HTPA with TPA as the probe, (d) quenching tests in the A-Boron/Fe^{III}/PDS system. (A-Boron 100 mg/L, initial pH 3.1, PDS 1.0 mM, Fe^{III} 20 μM, (a) BPA 20 μM, (b) DMPO 20 mM, (c) TPA 0.25 mM, (d) TBA or EtOH 100 mM, BPA 20 μM).

Table 1
Properties of ROS generated in the A-Boron/Fe^{III}/PDS system [20,21,35,36].

ROS	Redox potential	Lifetime	Rate constants, $M^{-1}\cdot s^{-1}$	
			TBA	EtOH
Hydroxyl radical, $^{\bullet}OH$	2.7 V	t = 20 ns	6×10^8	$(1.2–2.8) \times 10^9$
Sulfate radical, $SO_4^{\bullet-}$	2.5 ~ 3.1 V	t = 30 ~ 40 μs	8×10^5	$(1.6–7.7) \times 10^7$
Fe^{IV}-oxo complex, Fe (IV)	2.0 V	$t_{1/2}$ = 7 s	60	2.51×10^3

maintain high equilibrium concentration of Fe^{II}, which promotes the hydrolysis of Fe^{2+} to form $FeOH^+$ and further accelerates the generation of Fe(IV) (Scheme 1). Also, reaction solution pH can affect the oxidation capability and the proportion of radicals and Fe(IV). As shown in Fig. 3c, with initial pH increasing from 2.0 to 6.9, PMSO oxidation first increases and then decreases, reaching the peak of Δ[PMSO] = 140.0 μM at pH 3.6. The A-Boron/Fe^{III}/PDS system attains high oxidation capability at pH ranging from 2.5 to 4.3, and high concentration of hydroxyl can accelerate Fe(III) hydrolysis to precipitate iron(III) (hydr)oxides resulting in the decrease of oxidation capability at pH > 4.3. The proportion of Fe(IV)-induced oxidation of PMSO decreases from 67.5% at pH 2.0 to 51.5% at pH 5.6, due to the further hydrolysis of $FeOH^+$ to form $Fe(OH)_2$ and decrease the proportion of $FeOH^+$ derived Fe(IV) (Scheme 1). Therefore, the adjustment of solution pH and Fe^{III} dosage can regulate the oxidation capability and the proportion of nonradical and radical routes in the A-Boron/Fe^{III}/PDS system.

3.2.3. *Steady-state concentration of reactive oxygen species*

The steady-state concentrations of ROS generated in the A-Boron/Fe^{III}/PDS system for organics oxidation were then calculated based on a kinetic model [39]. Fig. S3 ~ S13 depict that pollutant oxidation in the A-Boron/Fe^{III}/PDS system follows a pseudo-first-order kinetic model

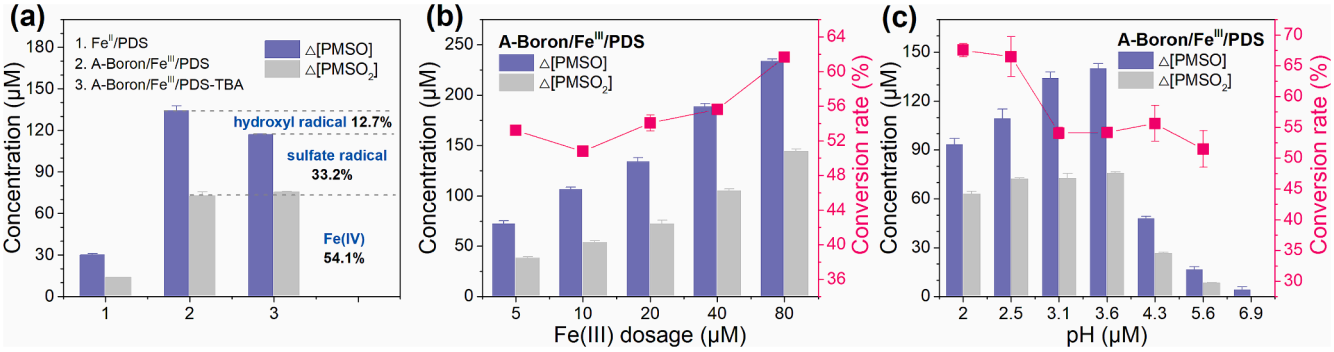

Fig. 3. Chemical probe analysis (PMSO). (a) contributions of $^{\bullet}OH$, $SO_4^{\bullet-}$, and Fe(IV) for PMSO oxidation, effect of (b) Fe(III) dosage and (c) initial pH on radical/nonradical pathways. (A-Boron 100 mg/L, PDS 1.0 mM, PMSO 0.5 mM, reaction time 30 min, (a) initial pH 3.1, Fe^{II} or Fe^{III} 20 μM, TBA 0 or 100 mM, (b) initial pH 3.1, Fe^{III} 5 ~ 80 μM, (c) initial pH 2.0 ~ 6.9, Fe^{III} 20 μM).

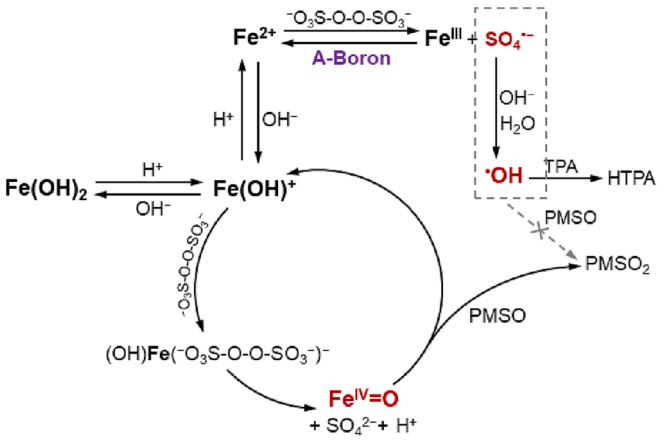

Scheme 1. Mechanism of chemical probe analysis of ROS in the A-Boron/Fe^{III}/PDS system.

($R^2 > 0.98$). Resulting from that $SO_4^{\cdot-}$, $^{\cdot}OH$, and Fe(IV) are the primary ROS, pollutant oxidation in the A-Boron/Fe^{III}/PDS system was described by Eq. (8), which can be further deduced into Eq. (9) by a natural logarithmic process.

$$-\frac{d[org]_t}{dt} = k_{(org,\ obs)}[org]_t = \left(k_{(org,\ \cdot OH)}[\cdot OH]_t + k_{(org,\ SO_4^{\cdot-})}[SO_4^{\cdot-}]_t + k_{(org,\ Fe(IV))}[Fe(IV)]_t\right)[org]_t \quad (8)$$

$$-\ln\frac{[org]_t}{[org]_0} = k_{(org,\ obs)}\,t = k_{(org,\ \cdot OH)}\int[\cdot OH]_t dt + k_{(org,\ SO_4^{\cdot-})}\int[SO_4^{\cdot-}]_t dt + k_{(org,\ Fe(IV))}\int[Fe(IV)]_t dt \quad (9)$$

where, $[org]_0$ is the dosage of organic contaminant, and $[org]_t$ is the instantaneous concentration of organic contaminants during reaction progress, respectively. $k_{(org,\ obs)}$ is the apparent rate constant of organic contaminant removal. $k_{(org,SO_4^{\cdot-})}$, $k_{(org,\ \cdot OH)}$, and $k_{(org,\ Fe(IV))}$ represent the second-order rate constants of these ROS induced oxidation of a specific organic contaminant, respectively.

$$k_{(org,\ obs)} = k_{(org,\ \cdot OH)}[\cdot OH]_{ss} + k_{(org,\ SO_4^{\cdot-})}[SO_4^{\cdot-}]_s + k_{(org,\ Fe(IV))}[Fe(IV)]_{ss} \quad (10)$$

The steady-state concentrations of Fe(IV) ($[Fe(IV)]_{ss} = \frac{1}{t}\int[Fe(IV)]_t dt$), sulfate radical ($[SO_4^{\cdot-}]_{ss} = \frac{1}{t}\int[SO_4^{\cdot-}]_t dt$), and hydroxyl radical ($[\cdot OH]_{ss} = \frac{1}{t}\int[\cdot OH]_t dt$) were then plugged into Eq. (9) to reveal the correlation between $k_{(org,\ obs)}$ and $[ROS]_{ss}$ (Eq. (10)), which are dependent on their second-order rate constants. PE, BA, and SMX were then applied as target organic contaminants with rate constants of $k_{(PE,\ \cdot OH)} = 6.6 \times 10^9\ M^{-1}{\cdot}s^{-1}$, $k_{(PE,\ SO_4^{\cdot-})} = 8.8 \times 10^9\ M^{-1}{\cdot}s^{-1}$, $k_{(PE,\ Fe(IV))} = 1.5 \times 10^4\ M^{-1}{\cdot}s^{-1}$, $k_{(BA,\ \cdot OH)} = 5.9 \times 10^9\ M^{-1}{\cdot}s^{-1}$, $k_{(BA,\ SO_4^{\cdot-})} = 1.2 \times 10^9\ M^{-1}{\cdot}s^{-1}$, $k_{(BA,\ Fe(IV))} = 80\ M^{-1}{\cdot}s^{-1}$, $k_{(SMX,\ \cdot OH)} = 5.5 \times 10^9\ M^{-1}{\cdot}s^{-1}$, $k_{(SMX,\ SO_4^{\cdot-})} = 3.0 \times 10^9\ M^{-1}{\cdot}s^{-1}$, $k_{(SMX,\ Fe(IV))} = 7.9 \times 10^4\ M^{-1}{\cdot}s^{-1}$ (Table S2) [13,40–44]. Moreover, $k_{(PE,\ obs)} = 0.26\ min^{-1}$, $k_{(SMX,\ obs)} = 0.19\ min^{-1}$, and $k_{(BA,\ obs)} = 0.09\ min^{-1}$ were calculated based on kinetic data for the oxidation of PE, SMX, and BA, respectively (Fig. S4 ~ S6). Therefore, $[SO_4^{\cdot-}]_{ss}$, $[\cdot OH]_{ss}$, and $[Fe(IV)]_{ss}$ were calculated by Cramer's rule, and $[Fe(IV)]_{ss} = \frac{\Delta_{Fe(IV)}}{\Delta} = 1.1 \times 10^{-8}$ M is approximately five orders of magnitude higher than $[SO_4^{\cdot-}]_{ss} = \frac{\Delta_{SO_4^{\cdot-}}}{\Delta} = 2.8 \times 10^{-13}$ M and $[\cdot OH]_{ss} = \frac{\Delta_{\cdot OH}}{\Delta} = 2.5 \times 10^{-13}$ M (Text S6).

3.2.4. Substrates specific reactivity

Hydroxyl radical with a high redox potential (2.7 V, Table 1) can non-selectively oxidize multifold organic contaminants with different structures ($>10^8\ M^{-1}{\cdot}s^{-1}$, Fig. 4a). Sulfate radical is an electrophilic ROS and can promptly degrade organic contaminants with electron-donating moieties (e.g., amidogen and phenolic hydroxyl group, Table S2) with higher kinetics ($>10^8\ M^{-1}{\cdot}s^{-1}$, Fig. 4a). Nevertheless, sulfate radical can also oxidize refractory contaminants with electron-withdrawing moieties (e.g., nitryl, chlorine, and ester, Table S2), albeit with lower rate constants ($10^5 \sim 10^8\ M^{-1}{\cdot}s^{-1}$, Fig. 4a). Generally, radicals ($SO_4^{\cdot-}$ and $^{\cdot}OH$) can degrade organic contaminants via electron transfer, addition elimination as well as hydrogen abstraction. However, their lifespans ($t(^{\cdot}OH) < 20$ ns and $t(SO_4^{\cdot-}) = 30 \sim 40$ μs, Table 1) are extremely short due to the quenching effects caused by co-existing substances in water (e.g., anions, metal ions, and natural organic matters) and self-quenching effect [20,21]. The short lifetime strongly reduces the effective diffusion of radical species especially in heterogenous AOTs. For instance, the majority of $^{\cdot}OH$ is consumed within 25 nm under nanoscale spatial confinement, and the concentration of $^{\cdot}OH$ immensely depends on the distance from the iron site of heterogenous Fenton reaction [45]. Nevertheless, Fe(IV) is a relatively stable reactive species in complex water matrixes with a significantly prolonged lifetime ($t_{1/2}$(Fe(IV)) = 7 s, Table 1). Fe(IV) is substrate sensitive and prefers to oxidize electron-rich moieties of organic contaminants via electron-, oxygen-, hydrogen-, and hydride-transfer reactions as well as electrophilic addition; the corresponding reactivity and reaction pathways are different from free radicals [11–13]. Therefore, Fe(IV) cannot degrade the refractory contaminants (e.g., phthalates, nitrobenzenes, and benzoic acids), but Fe(IV)-induced oxidation of electron-rich contaminants attains high ROS utilization efficiency and requires significantly reduced chemical input [11–13].

To our delight, the A-Boron/Fe^{III}/PDS system overcomes the drawbacks of individual ROS-dominated oxidation systems and can effectively degrade a large variety of organic contaminants by simultaneously producing reactive radicals and Fe(IV). Fig. 4b depicts that the A-Boron/Fe^{III}/PDS system can significantly degrade 11 kinds of organic contaminants, including phenols (PE and BPA), phthalates (DEP and DMP), drugs (SMX and IBP), antibiotic (TC) as well as dyes (RB and MB). However, the A-Boron/Fe^{III}/PDS system also shows substrate-dependent reactivity, thus Fig. 4c shows the significant difference of k_{obs} ($0.03\ min^{-1} \sim 0.26\ min^{-1}$) for the oxidation of different organic contaminants. The A-Boron/Fe^{III}/PDS system exhibits the relative low oxidation capabilities to oxidize the more refractory organic contaminants (DMP (72.9%, $0.03\ min^{-1}$), DEP (78.1%, $0.04\ min^{-1}$), BA (93.3%, $0.09\ min^{-1}$), NB (75.7%, $0.04\ min^{-1}$)), and meanwhile, other 6 contaminants with electron-donating moieties (PE ($0.26\ min^{-1}$), BPA ($0.25\ min^{-1}$), SMX ($0.19\ min^{-1}$), IBP ($0.19\ min^{-1}$), TC ($0.22\ min^{-1}$), RB ($0.21\ min^{-1}$), MB ($0.22\ min^{-1}$)) can be promptly and entirely degraded within 20 min (Fig. 4b-4c and Fig. S3 ~ S13).

The frontier orbital energies (E_{HOMO}, E_{LUMO}, and $\Delta E = E_{LUMO} - E_{HOMO}$) can indicate the oxidation of organic contaminants by setting up a QSAR model between frontier orbital energies and k_{obs} [46,47]. However, these QSAR models are generally applied in single-ROS-dominated oxidation (e.g., hydroxyl radical and sulfate radical), but not for an oxidation system with multiple reactive species [48,49]. The frontier orbital energies of above 11 organic contaminants were obtained based on quantum chemical calculations (Table 2), which were then fitted with k_{obs} of these organic contaminants. Fig. 4d ~ 4f demonstrate that k_{obs} of these organic contaminants are linearly related to E_{HOMO} with a high correlation coefficient ($R^2 = 0.95$, $k_{obs} = 0.13E_{HOMO} + 1.01$), but not for E_{LUMO} or ΔE. The value of E_{HOMO} represents the electron-donation capability of the organic molecule [50]. Therefore, although Fe(IV) and reactive radicals ($SO_4^{\cdot-}$ and $^{\cdot}OH$) exhibit substrate-specific reactivity in degrading these organic pollutants, the overall apparent k_{obs} values depend on the electron-donation capabilities of organics in the A-Boron/Fe^{III}/PDS system.

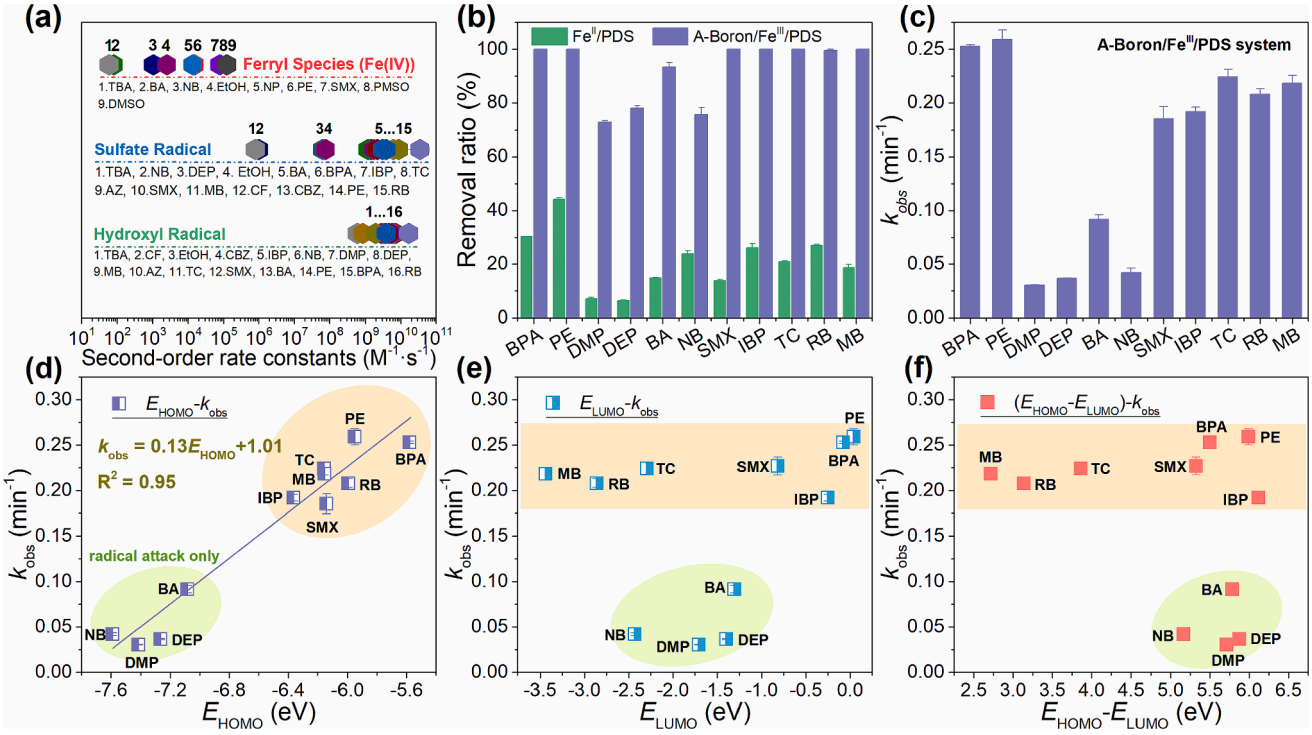

Fig. 4. Performance of the A-Boron/Fe^{III}/PDS systems toward diverse organic contaminants. (a) second-order rate constants between ROS and various contaminants, (b) ratios and (c) k_{obs} of contaminants removal, relationship between k_{obs} and (d) E_{HOMO}, (e) E_{LUMO}, and (f) ΔE (E_{LUMO} - E_{HOMO}). (Initial pH 3.1, PDS 1.0 mM, Fe^{II} or Fe^{III} 20 μM, A-Boron 100 mg/L, organics 20 μM).

3.3. Mechanism investigation

3.3.1. Kinetic equilibrium of Fe^{III}/Fe^{II} conversion

Fe^{II} is the critical iron species for the fast heterolysis of peroxide bonds of PDS to generate ROS. However, the rate-determining step during iron-catalyzed chain reactions is Fe^{II} regeneration (Eqs. (1)–(5)) [15]. The Fe^{III}/Fe^{II} transitions were analyzed by XPS and NEXAFS as well as monitoring iron species in the solution to unveil the role of A-Boron. Fe 2p XPS spectrum in Fig. 5a reveals that no particular signal of iron species was detected on the surface of original A-Boron, while specific peaks of both Fe^{II} (Fe $2p_{1/2}$ 711.1 eV and Fe $2p_{3/2}$ 725.1 eV) and Fe^{III} (Fe $2p_{1/2}$ 715.6 eV and Fe $2p_{3/2}$ 730.1 eV) were detected on the surface of residual A-Boron after the cyclic tests [51,52]. Meanwhile, Fe^{II} (L_2-edge at 721.5 eV and L_3-edge at 708.3 eV) and Fe^{III} (L_2-edge at 724.1 eV and L_3-edge at 711.4 eV) were also detected in the NEXAFS spectra after the oxidation reaction (Fig. S14) [53]. The high proportion of Fe^{II} on the surface of residual A-Boron (Fig. 5a) demonstrates the effective transformation from Fe^{III} into Fe^{II} at the surface region of A-Boron.

$$2B^0 + 6Fe^{III} + 3H_2O \rightarrow B_2O_3 + 6Fe^{II} + 6H^+ \quad (11)$$

For further investigating the interaction between A-Boron and Fe^{III}, the transformation of iron species was analyzed in various systems. As shown in Fig. 5b, nearly 65% Fe^{II} was converted to Fe^{III} in 1 min, and Fe^{II} was completely oxidized into Fe^{III} in 5 min in the Fe^{II}/PDS system. The sluggish recovery of Fe^{II} causes the low oxidation rate in the Fe^{II}/PDS system at the second stage [8]. However, Fe^{III} was completely converted to Fe^{II} in the A-Boron/Fe^{III} system within 1 min in the absence of PDS, revealing the high electron-donating capability of A-Boron for the rapid reduction of Fe^{III}. The concentration of soluble Fe^{II} maintains kinetic equilibrium resulting from fast Fe^{III} reduction (Eq. (11)) and subsequent Fe^{II} oxidation (Eqs. (1) and (4)) in the A-Boron/Fe^{III}/PDS system [8,11]. >5.0 μM Fe^{III} was rapidly transformed into Fe^{II}. Then, the concentration of Fe^{II} kept relatively steady between 5.0 and 7.0 μM to guarantee the fast Fenton-like kinetics to continuously produce multiple ROS in the A-Boron/Fe^{III}/PDS system. Moreover, the low XPS (Fig. 5a) and NEXAFS (Fig. S14) intensities of Fe species on the surface of residual A-Boron and a small proportion of surface iron species (Fig. 5b) demonstrate that Fe^{III} can be reduced into Fe^{II} which will be further released into the solution. ROS are primarily produced via Fe^{II}-mediated homogeneous activation of PDS.

3.3.2. Route of boron species induced sustainable Fe^{III} reduction

The HRTEM image of original A-Boron in Fig. S15 reveals that A-Boron is a short-range-ordered and long-range-disordered material, which is largely distinct from crystalline boron powder with clear crystal structure [38]. Boron crystal consists of B_{12} icosahedra by three-center-two-electrons/two-center-two-electrons boron-boron bonds between and in the B_{12} icosahedron, which perfectly addresses shortcoming of electron-deficient property of boron atoms with three valence electrons [23–26]. Some crystalline regions on the A-Boron surface with lattice spacings of 0.82 nm and 0.42 nm were discovered, and other disorder-packed domains are spotted among these crystalline regions [29]. Moreover, the regions of surface impurities also illustrate that A-Boron surface is covered by a suboxide/oxide boron layer.

The high-resolution B 1s profile of original A-Boron in Fig. S16 is fitted into boron-boron bonds (70.2% B^0, 187.3 eV), interfacial suboxide boron (28.2% B^I and B^{II}, 188.7 eV), and boron oxide (1.6% B^{III}, 190.8 eV) [54]. The existence of low valent boron species is also verified based on the EPR analysis of A-Boron [29]. Fig. 5c depicts the existence of abundant unpaired electrons in pristine A-Boron. The surface boron species of A-Boron possess rich electrons for fast Fe^{III} reduction. After oxidation, the intensity of unpaired electrons of A-Boron decreases in the A-Boron/Fe^{III}/PDS system.

Moreover, Fig. 4d and S16-S18 depict that the percentages of intact boron-boron bonds decrease to 67.4% after one cycling test and 61.5% after five cycling tests; meanwhile, the proportion of interfacial suboxide boron increases to 30.6% and 36.5%, respectively. The stepwise oxidation with the cleavage of semi-metallic boron-boron bonds accompanies with the electron donation to realize fast Fe^{III} reduction.

Table 2
Frontier orbital energies of organic contaminants.

Organic contaminants	E_{LOMO} (eV)		E_{HOMO} (eV)		$\Delta E = E_{LUMO}$-E_{HOMO} (eV)
BPA	−0.079	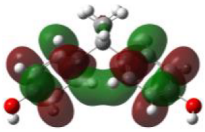	−5.579	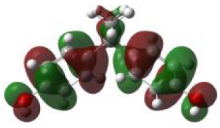	5.500
PE	0.038	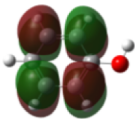	−5.953		5.991
DMP	−1.707	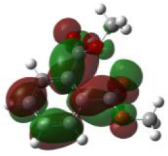	−7.415	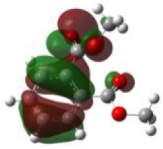	5.708
DEP	−1.395	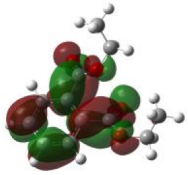	−7.267	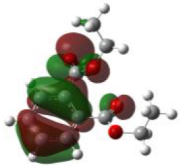	5.872
BA	−1.305	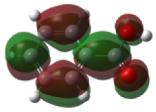	−7.085	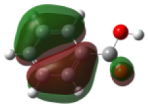	5.780
NB	−2.429	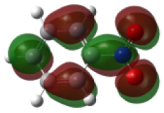	−7.590	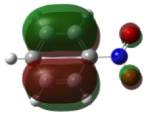	5.161
SMX	−0.820	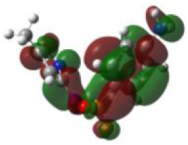	−6.143	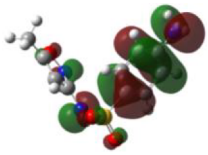	5.323
IBP	−0.252	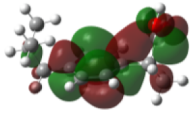	−6.365	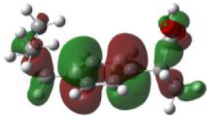	6.112
TC	−2.295	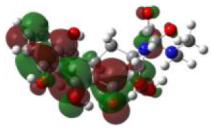	−6.156	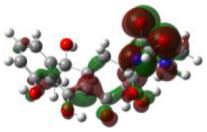	3.862
RB	−2.862	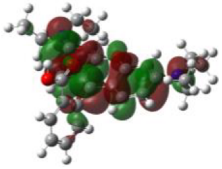	−5.995	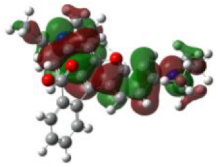	3.134
MB	−3.438		−6.154	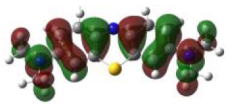	2.716

Thus, the surface crystalline structure of A-Boron was partially destroyed with the increase of amorphous regions (Fig. S15). Nonetheless, the residual A-Boron after ten cycles still possesses a high capability to rapidly reduce Fe^{III} to Fe^{II} within 1 min (Fig. S19).

For further analyzing the role of interfacial suboxide boron, THDB ($(OH)_2$-B-B-$(OH)_2$, B^{II}) as a model molecular was employed to identify the reduction capability of interfacial suboxide boron species [54]. Fig. 5e depicts that THDB can also fleetly convert Fe^{III} to Fe^{II} in the THDB/Fe^{III} system, and Fe^{II} concentration also maintains the kinetic equilibrium around 7.0 μM in the THDB/Fe^{III}/PDS system. Moreover, as illustrated in Fig. 5f, although THDB cannot directly activate PDS to degrade BPA, the THDB/Fe^{III}/PDS system attains 100% BPA removal in

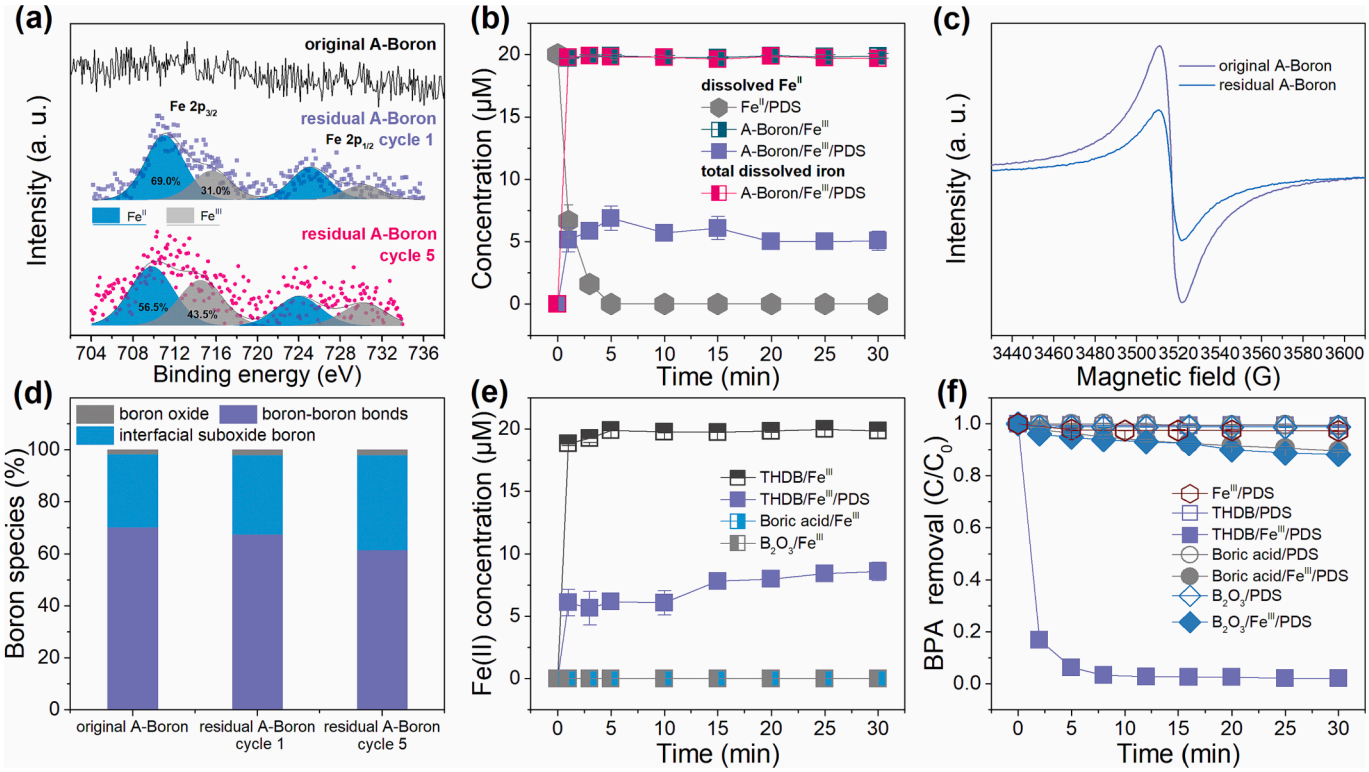

Fig. 5. Boron species induced fast Fe^{III} reduction. (a) Fe 2p XPS spectra of original and residual A-Boron, (b) transformation of Fe species, (c) EPR analysis and (d) B 1s XPS spectra of original and residual A-Boron, (e) suboxide and oxide boron species induced Fe^{III} reduction, (f) suboxide and oxide boron species mediated Fe^{III}/PDS systems. (Initial pH 3.1, PDS 1.0 mM, Fe^{II} or Fe^{III} 20 μM, A-Boron or boron species (THDB, boric acid, and boron oxide) 100 mg/L, BPA 20 μM).

10 min. Also, the interfacial suboxide boron derived from pristine boron can still reduce Fe^{III} to Fe^{II} rapidly and further accelerate Fenton-like reactions to produce ROS. Meanwhile, suboxide boron was converted to boron oxide.

$$B_2O_3 + 6H_2O \rightarrow 2H_3BO_3 + 6H^+ \quad (12)$$

Boron oxide (B^{III}) derived from further oxidation of suboxide boron species is the highest valent state of boron species, which cannot further reduce Fe^{III} into Fe^{II} (Fig. 5e) to drive the Fe^{III}/PDS system (Fig. 5f). However, boron oxide can be fleetly dissolved into boric acid (Eq. (12)) to expose fresh surface boron. Thus self-cleaned A-Boron surface will sustainably provide fresh and reactive boron sites for fast Fe^{III} reduction and contaminant oxidation. Thus Fig. 5c and S18 depict that the proportion of boron oxide after five cycling tests is merely 2.0%. The XRD spectra in Fig. S20 also reveal the continuing exposure of surface crystalline boron during cyclic tests. Therefore, A-Boron exhibits excellent reactivity to boost the Fe^{III}/PDS system and promptly oxidize BPA within 20 min for multiple runs (Fig. 1c), and the A-Boron/Fe^{III}/PDS system largely immunes from complex background factors in real water matrixes (Fig. S21 and S22).

In addition, the BPA removal profiles match well with the pseudo-first order kinetic model in the A-Boron/Fe^{III}/PDS system at different experimental conditions (R^2 = 0.99, Fig. S2). The apparent kinetic model of BPA removal was then simulated as Eq. (13) by investigating the dosing effects of PDS, Fe^{III}, and A-Boron on BPA removal (Text S7, Fig. S23 ~ S25, and Table S3 ~ S5). The reaction orders of PDS (0.81) and Fe^{III} (0.81) are about 2.5 times higher than that of A-Boron (0.28), suggesting that the self-cleaning effect and high reduction capabilities of original boron-boron bonds and interfacial suboxide boron provided the abundant reductive sites on A-Boron for fast Fe^{III} reduction. Therefore, the dosage of A-Boron is less sensitive for BPA oxidation than the loadings of PDS and Fe^{III}.

$$k_{obs} = 11.43[\text{A-Boron}]_0^{0.28}[Fe^{III}]_0^{0.81}[PDS]_0^{0.81} \quad (13)$$

3.4. BPA degradation pathway

Fukui indexes can indicate the potential sites of the oxidation of organic compounds via electrophilic (f_A^-), nucleophilic (f_A^+), and radical (f_A^0) reactions [55]. Therefore, NPA charges and Fukui indexes of BPA were computed in Table 3 to analyze BPA oxidation via electrophilic attack by Fe(IV) and radical attack by $SO_4^{\bullet-}$ and $^{\bullet}OH$. Moreover, intermediates derived from BPA oxidation were also qualitatively detected using UHPLC-QTOF-MS (Table S6 and Fig. S26 ~ S34).

Based on theoretical and experimental results, radicals ($SO_4^{\bullet-}$ and $^{\bullet}OH$) and Fe(IV) caused degradation pathways of BPA in the A-Boron/Fe^{III}/PDS system are proposed involving three stages (Scheme 2) [55,56]. In the first stage, BPA can be oxidized via three routes: (1) sulfate radical abstracts electron of carbon atoms (C12 ~ C15) to form IP1, which further converts to TP1 and TP2 (route 1); (2) hydroxyl radical induces the hydroxylation of BPA at C12 ~ C15 to produce TP1 and TP2 (route 2); (3) sulfate radical or Fe(IV) abstracts hydrogen atoms of phenolic hydroxyl groups (O1 and O2) via electrophilic attack to form IP3, and the subsequent decomposition of IP3 can produce monocyclic aromatic compounds (TP6 and TP8) (route 3). Due to the high

Table 3
Natural population analysis (NPA) charges and Fukui index of BPA based on DFT calculation.

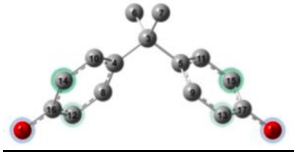

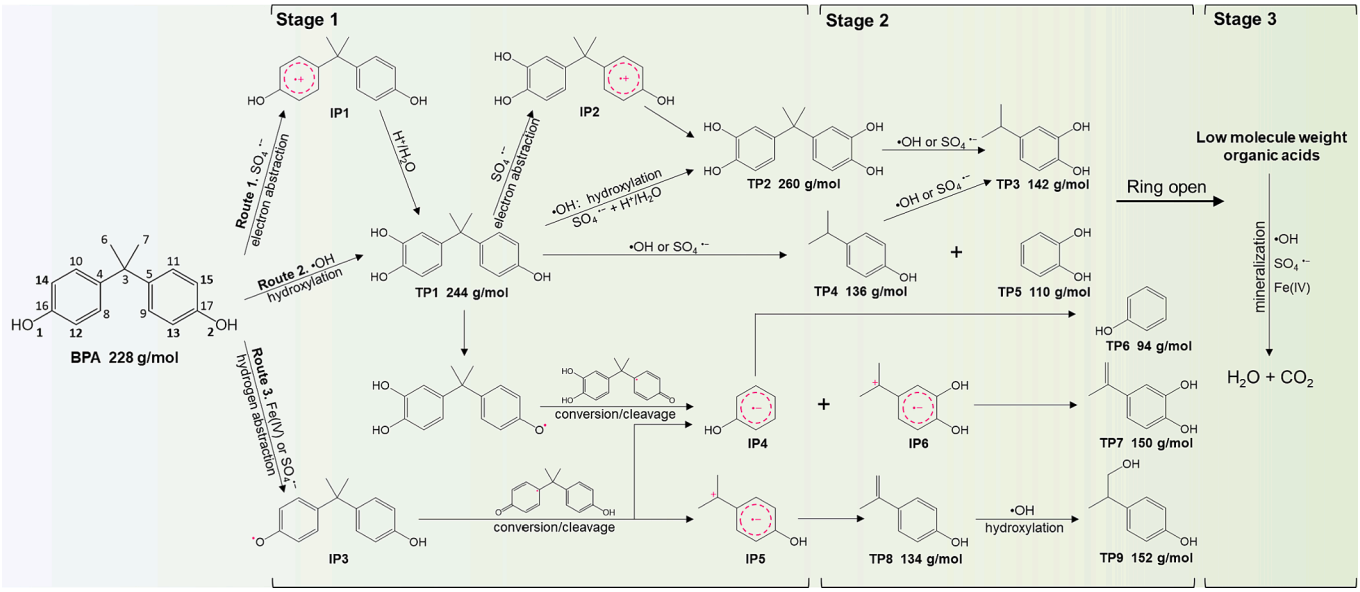

Scheme 2. BPA degradation pathways in the A-Boron/Fe^{III}/PDS system.

proportion of Fe(IV) for organic contaminant oxidation (Fig. 3a), Fe(IV) induced route 3 may be the primary approach for BPA oxidation at the first stage. In stage 2, intermediates derived from stage 1 were further oxidized to phenolics (TP3 ~ TP9) by hydroxyl radical (hydroxylation), sulfate radical (electron abstract), and Fe(IV) (hydrogen abstract). Moreover, the further oxidation of these phenolics by cleaving aromatic rings can generate low-molecular-weight organic molecules (e.g., oxalic acid and maleic acid), which will be mineralized to water and carbon dioxide subsequently (stage 3).

4. Conclusion

In this study, we found that metal-free A-Boron can serve as an effective co-catalyst to boost iron-catalyzed Fenton-like activation of PDS. Due to the simultaneous generation of reactive radicals ($SO_4^{\bullet-}$ and $^{\bullet}OH$) and Fe(IV), the A-Boron/Fe^{III}/PDS system can degrade a variety of contaminants. However, the A-Boron/Fe^{III}/PDS system shows substrate-specific reactivity, and k_{obs} values of organics linearly depend on their E_{HOMO} based on QSAR and DFT calculations. The proportions of non-radical and radical for contaminant oxidation were identified by the chemical probe of PMSO. Mechanism investigation reveals that the stepwise oxidation of A-Boron from semi-metallic boron-boron bonds (B^0) to suboxide boron (B^I and B^{II}) and boron oxide (B^{III}) to donate electrons for Fe^{III} reduction continuously. The concentration of Fe^{II} maintains a dynamic equilibrium between 5.0 μM to 7.0 μM for sustainable Fenton-like reactions to generate ROS. Moreover, the self-cleaning behavior of A-Boron will maintain a reactive surface for long-lasting operation for up to 10 cycles without apparent performance decline. In addition, the BPA oxidation routes in the A-Boron/Fe^{III}/PDS system are proposed involving three stages based on Fukui index and UHPLC-QTOF-MS analyses. Although the economic cost of the A-Boron boosted Fenton-like technologies for practical application requiring further evaluation, this study successfully provides a metal-free and stable co-catalyst to enable long-lasting Fenton-like oxidation for water remediation.

CRediT authorship contribution statement

Peng Zhou: Conceptualization, Methodology, Investigation, Data curation, Writing – original draft, Funding acquisition, Writing – review & editing. **Shuang Meng:** Investigation, Data curation. **Minglu Sun:** Investigation, Data curation. **Kunsheng Hu:** Investigation, Methodology. **Yangyang Yang:** Investigation, Methodology. **Bo Lai:** Project administration, Writing – review & editing. **Shaobin Wang:** Project administration, Writing – review & editing. **Xiaoguang Duan:** Conceptualization, Methodology, Supervision, Validation, Resources, Project administration, Funding acquisition, Writing – review & editing.

Declaration of Competing Interest

The authors declare that they have no known competing financial interests or personal relationships that could have appeared to influence the work reported in this paper.

Acknowledgements

This work was financially supported by Australian Research Council (DE210100253), Natural Science Foundation of Sichuan Province (2022NSFSC0972) and National Natural Science Foundation of China (22106110).

Appendix A. Supplementary data

Supplementary data to this article can be found online at https://doi.org/10.1016/j.seppur.2023.123860.

References

[1] Z. Yu, H. Rabiee, J. Guo, Synergistic effect of sulfidated nano zerovalent iron and persulfate on inactivating antibiotic resistant bacteria and antibiotic resistance genes, Water Res. 198 (2021) 117141.
[2] S. Nimai, H. Zhang, Z. Wu, N. Li, B. Lai, Efficient degradation of sulfamethoxazole by acetylene black activated peroxydisulfate, Chinese Chem. Lett. 31 (2020) 2657–2660.
[3] P. Zhou, J. Zhang, Y. Zhang, G. Zhang, W. Li, C. Wei, J. Liang, Y. Liu, S. Shu, Degradation of 2,4-dichlorophenol by activating persulfate and peroxomonosulfate using micron or nanoscale zero-valent copper, J. Hazard. Mater. 344 (2018) 1209–1219.
[4] J. Lee, U. von Gunten, J.H. Kim, Persulfate-Based Advanced Oxidation: Critical Assessment of Opportunities and Roadblocks, Environ. Sci. Technol. 54 (2020) 3064–3081.
[5] X. Duan, H. Sun, S. Wang, Metal-Free Carbocatalysis in Advanced Oxidation Reactions, Acc. Chem. Res. 51 (2018) 678–687.
[6] W. Ren, C. Cheng, P. Shao, X. Luo, H. Zhang, S. Wang, X. Duan, Origins of Electron-Transfer Regime in Persulfate-Based Nonradical Oxidation Processes, Environ. Sci. Technol. 56 (2022) 78–97.
[7] L. Qiao, Y. Shi, Q. Cheng, B. Liu, J. Liu, The removal efficiencies and mechanism of aniline degradation by peroxydisulfate activated with magnetic Fe-Mn oxides composite, J. Water Reuse Desal. 11 (2021) 212–223.

[8] Y.F. Rao, L. Qu, H. Yang, W. Chu, Degradation of carbamazepine by Fe(II)-activated persulfate process, J. Hazard. Mater. 268 (2014) 23–32.
[9] J.P. Zhu, Y.L. Lin, T.Y. Zhang, T.C. Cao, B. Xu, Y. Pan, X.T. Zhang, N.Y. Gao, Modelling of iohexol degradation in a Fe(II)-activated persulfate system, Chem. Eng. J. 367 (2019) 86–93.
[10] B. Liu, F. Qu, W. Chen, H. Liang, T. Wang, X. Cheng, H. Yu, G. Li, B. Van der Bruggen, Microcystis aeruginosa-laden water treatment using enhanced coagulation by persulfate/Fe(II), ozone and permanganate: Comparison of the simultaneous and successive oxidant dosing strategy, Water Res. 125 (2017) 72–80.
[11] Z. Wang, J. Jiang, S. Pang, Y. Zhou, C. Guan, Y. Gao, J. Li, Y. Yang, W. Qiu, C. Jiang, Is Sulfate Radical Really Generated from Peroxydisulfate Activated by Iron(II) for Environmental Decontamination? Environ. Sci. Technol. 52 (2018) 11276–11284.
[12] Z. Wang, W. Qiu, S.Y. Pang, Q. Guo, C.T. Guan, J. Jiang, Aqueous Iron(IV)-Oxo Complex: An Emerging Powerful Reactive Oxidant Formed by Iron(II)-Based Advanced Oxidation Processes for Oxidative Water Treatment, Environ. Sci. Technol. 56 (2022) 1492–1509.
[13] H. Dong, Y. Li, S. Wang, W. Liu, G. Zhou, Y. Xie, X. Guan, Both Fe(IV) and Radicals Are Active Oxidants in the Fe(II)/Peroxydisulfate Process, Environ. Sci. Technol. Lett. 7 (2020) 219–224.
[14] S. Meng, P. Zhou, Y. Sun, P. Zhang, C. Zhou, Z. Xiong, H. Zhang, J. Liang, B. Lai, Reducing agents enhanced Fenton-like oxidation (Fe(III)/Peroxydisulfate): Substrate specific reactivity of reactive oxygen species, Water Res. 218 (2022) 118412.
[15] H. Zhou, H. Zhang, Y. He, B. Huang, C. Zhou, G. Yao, B. Lai, Critical review of reductant-enhanced peroxide activation processes: Trade-off between accelerated Fe^{3+}/Fe^{2+} cycle and quenching reactions, Appl. Catal. B: Environ. 286 (2021) 119900.
[16] L. Chen, J. Ma, X. Li, J. Zhang, J. Fang, Y. Guan, P. Xie, Strong enhancement on fenton oxidation by addition of hydroxylamine to accelerate the ferric and ferrous iron cycles, Environ. Sci. Technol. 45 (2011) 3925–3930.
[17] J. Li, Y. Wan, Y. Li, G. Yao, B. Lai, Surface Fe(III)/Fe(II) cycle promoted the degradation of atrazine by peroxymonosulfate activation in the presence of hydroxylamine, Appl. Catal. B: Environ. 256 (2019) 117782.
[18] P. Zhou, J. Zhang, Y. Zhang, Y. Liu, J. Liang, B. Liu, W. Zhang, Generation of hydrogen peroxide and hydroxyl radical resulting from oxygen-dependent oxidation of l-ascorbic acid via copper redox-catalyzed reactions, RSC Adv. 6 (2016) 38541–38547.
[19] Y. Qin, F. Song, Z. Ai, P. Zhang, L. Zhang, Protocatechuic Acid Promoted Alachlor Degradation in Fe(III)/H_2O_2 Fenton System, Environ. Sci. Technol. 49 (2015) 7948–7956.
[20] G.V. Buxton, C.L. Greenstock, W.P. Helman, A.B. Ross, Critical-Review of Rate Constants for Reactions of Hydrated Electrons, Hydrogen-Atoms and Hydroxyl Radicals ((•OH/•O−) in Aqueous-Solution, J. Phys. Chem. Ref. Data 17 (1988) 513–886.
[21] P. Neta, R.E. Huie, A.B. Ross, Rate Constants for Reactions of Inorganic Radicals in Aqueous-Solution, J. Phys. Chem. Ref. Data 17 (1988) 1027–1284.
[22] H.F. Schaefer, F.E. Harris, Electronic Structure of Atomic Boron, Phys. Rev. 167 (1968) 67–73.
[23] Z.H. Zhang, E.S. Penev, B.I. Yakobson, Two-dimensional boron: structures, properties and applications, Chem. Soc. Rev. 46 (2017) 6746–6763.
[24] T. Ogitsu, E. Schwegler, G. Galli, β-Rhombohedral boron: at the crossroads of the chemistry of boron and the physics of frustration, Chem. Rev. 113 (2013) 3425–3449.
[25] B. Albert, H. Hillebrecht, Boron: elementary challenge for experimenters and theoreticians, Angew. Chem. Int. Ed. 48 (2009) 8640–8668.
[26] J. He, E. Wu, H. Wang, R. Liu, Y. Tian, Ionicities of boron-boron bonds in B_{12} icosahedra, Phys. Rev. Lett. 94 (2005) 015504.
[27] P. Zhou, W. Ren, G. Nie, X. Li, X. Duan, Y. Zhang, S. Wang, Fast and Long-Lasting Iron(III) Reduction by Boron Toward Green and Accelerated Fenton Chemistry, Angew. Chem. Int. Ed. 59 (2020) 16517–16526.
[28] P. Zhou, F. Cheng, G. Nie, Y.Y. Yang, K.S. Hu, X.G. Duan, Y.L. Zhang, S.B. Wang, Boron carbide boosted Fenton-like oxidation: A novel Fe(III)/Fe(II) circulation, Green Energy Environ. 5 (2020) 414–422.
[29] X. Duan, W. Li, Z. Ao, J. Kang, W. Tian, H. Zhang, S.H. Ho, H. Sun, S. Wang, Origins of boron catalysis in peroxymonosulfate activation and advanced oxidation, J. Mater. Chem. A 7 (2019) 23904–23913.
[30] X. Li, K. Hu, Y. Huang, Q. Gu, Y. Chen, B. Yang, R. Qiu, W. Luo, B.M. Weckhuysen, K. Yan, Upcycling biomass waste into Fe single atom catalysts for pollutant control, J. Energy Chem. 69 (2022) 282–291.
[31] S.Z. Pei, S.J. You, J. Ma, X.D. Chen, N.Q. Ren, Electron Spin Resonance Evidence for Electro-generated Hydroxyl Radicals, Environ. Sci. Technol. 54 (2020) 13333–13343.
[32] M.A. Cashman, L. Kirschenbaum, J. Holowachuk, T.B. Boving, Identification of hydroxyl and sulfate free radicals involved in the reaction of 1,4-dioxane with peroxone activated persulfate oxidant, J. Hazard. Mater. 380 (2019) 120875.
[33] H. Yin, J. Li, H. Yan, H. Cai, Y. Wan, G. Yao, Y. Guo, B. Lai, Activation of peroxymonosulfate by $CuCo_2O_4$ nano-particles towards long-lasting removal of atrazine, J. Water Reuse Desal. 11 (2021) 542–559.
[34] P.H. Shao, J.Y. Tian, B.R. Liu, W.X. Shi, S.S. Gao, Y.L. Song, M. Ling, F.Y. Cui, Morphology-tunable ultrafine metal oxide nanostructures uniformly grown on graphene and their applications in the photo-Fenton system, Nanoscale 7 (2015) 14254–14263.
[35] O. Pestovsky, A. Bakac, Aqueous ferryl(IV) ion: Kinetics of oxygen atom transfer to substrates and oxo exchange with solvent water, Inorg. Chem. 45 (2006) 814–820.
[36] D.N. Zhou, H. Zhang, L. Chen, Sulfur-replaced Fenton systems: can sulfate radical substitute hydroxyl radical for advanced oxidation technologies? J. Chem. Technol. Biot. 90 (2015) 775–779.
[37] Z. Wang, W. Qiu, S.Y. Pang, Y. Zhou, Y. Gan, C.T. Guan, J. Jiang, Further understanding the involvement of Fe(IV) in peroxydisulfate and peroxymonosulfate activation by Fe(II) for oxidative water treatment, Chem. Eng. J. 371 (2019) 842–847.
[38] P. Zhou, Y. Yang, W. Ren, X. Li, Y. Zhang, B. Lai, S. Wang, X. Duan, Molecular and kinetic insights to boron boosted Fenton-like activation of peroxymonosulfate for water decontamination, Appl. Catal. B: Environ. 319 (2022) 121916.
[39] W. Ren, P. Zhou, G. Nie, C. Cheng, X. Duan, H. Zhang, S. Wang, Hydroxyl radical dominated elimination of plasticizers by peroxymonosulfate on metal-free boron: Kinetics and mechanisms, Water Res. 186 (2020) 116361.
[40] M.E. Lindsey, M.A. Tarr, Inhibition of hydroxyl radical reaction with aromatics by dissolved natural organic matter, Environ. Sci. Technol. 34 (2000) 444–449.
[41] J. Ziajka, W. Pasiuk-Bronikowska, Rate constants for atmospheric trace organics scavenging $SO_4^{\bullet-}$ in the Fe-catalysed autoxidation of S(IV), Atmos. Environ. 39 (2005) 1431–1438.
[42] L. Wojnárovits, E. Takács, Rate constants of sulfate radical anion reactions with organic molecules: A review, Chemosphere 220 (2019) 1014–1032.
[43] Y. Lee, D. Gerrity, M. Lee, A.E. Bogeat, E. Salhi, S. Gamage, R.A. Trenholm, E. C. Wert, S.A. Snyder, U. von Gunten, Prediction of micropollutant elimination during ozonation of municipal wastewater effluents: use of kinetic and water specific information, Environ. Sci. Technol. 47 (2013) 5872–5881.
[44] C. Luo, M. Feng, T. Zhang, V.K. Sharma, C.H. Huang, Ferrate(VI) Oxidation of Pharmaceuticals in Hydrolyzed Urine: Enhancement by Creatinine and the Role of Fe(IV), ACS ES&T Water 1 (2021) 969–979.
[45] S. Zhang, M. Sun, T. Hedtke, A. Deshmukh, X. Zhou, S. Weon, M. Elimelech, J. H. Kim, Mechanism of Heterogeneous Fenton Reaction Kinetics Enhancement under Nanoscale Spatial Confinement, Environ. Sci. Technol. 54 (2020) 10868–10875.
[46] R. Xiao, T. Ye, Z. Wei, S. Luo, Z. Yang, R. Spinney, Quantitative Structure-Activity Relationship (QSAR) for the Oxidation of Trace Organic Contaminants by Sulfate Radical, Environ. Sci. Technol. 49 (2015) 13394–13402.
[47] X. Li, Z. Yang, G. Wu, Y. Huang, Z. Zheng, H.F. Garces, K. Yan, Fabrication of ultrathin lily-like $NiCo_2O_4$ nanosheets via mooring NiCo bimetallic oxide on waste biomass-derived carbon for highly efficient removal of phenolic pollutants, Chem. Eng. J. 441 (2022).
[48] G.D. Fang, D.D. Dionysiou, Y. Wang, S.R. Al-Abed, D.M. Zhou, Sulfate radical-based degradation of polychlorinated biphenyls: effects of chloride ion and reaction kinetics, J. Hazard. Mater. 227–228 (2012) 394–401.
[49] Z. Yang, S. Luo, Z. Wei, T. Ye, R. Spinney, D. Chen, R. Xiao, Rate constants of hydroxyl radical oxidation of polychlorinated biphenyls in the gas phase: A single-descriptor based QSAR and DFT study, Environ. Pollut. 211 (2016) 157–164.
[50] K. Takahashi, S. Ito, R. Shintani, K. Nozaki, Selective synthesis of unsymmetric dibenzo[a, e]pentalenes by a rhodium-catalysed stitching reaction, Chem. Sci. 8 (2017) 101–107.
[51] P. Zhou, J. Zhang, Z. Xiong, Y. Liu, X. Huo, X. Cheng, W. Li, F. Cheng, Y. Zhang, C_{60} Fullerol promoted Fe(III)/H_2O_2 Fenton oxidation: Role of photosensitive Fe(III)-Fullerol complex, Appl. Catal. B: Environ. 265 (2020) 118264.
[52] S. Zou, Q. Chen, Y. Liu, Y. Pan, G. Yao, Z. Pan, B. Lai, The capacity and mechanisms of various oxidants on regulating the redox function of ZVI, Chinese Chem. Lett. 32 (2021) 2066–2072.
[53] M. Maric, M. Sohail, R. De Marco, A near edge X-ray absorption fine structure (NEXAFS) study of the response mechanism of the iron(III) chalcogenide glass membrane ion-selective electrode, Electrochem. Commun. 41 (2014) 27–30.
[54] C.W. Ong, H. Huang, B. Zheng, R.W.M. Kwok, Y.Y. Hui, W.M. Lau, X-ray photoemission spectroscopy of nonmetallic materials: Electronic structures of boron and B_xO_y, J. Appl. Phys. 95 (2004) 3527–3534.
[55] J. Wang, M. Zheng, Y. Deng, M. Liu, Y. Chen, N. Gao, E. Du, W. Chu, H. Guo, Generality and diversity on the kinetics, toxicity and DFT studies of sulfate radical-induced transformation of BPA and its analogues, Water Res. 219 (2022) 118506.
[56] G. Kyrila, A. Katsoulas, V. Schoretsaniti, A. Rigopoulos, E. Rizou, S. Doulgeridou, V. Sarli, V. Samanidou, M. Touraki, Bisphenol A removal and degradation pathways in microorganisms with probiotic properties, J. Hazard. Mater. 413 (2021) 125363.